Concealed Object Discrimination in Forested Areas Using PolTomoSAR with Various Baseline Configurations

Youssra El Bennioui[1], Laurent Ferro-famil[1,2], Yue Huang[3]

[1] ISAE-Supaero, 31400, Toulouse, France
[2] CESBIO, University of Toulouse, 31400, Toulouse, France
[3] Meteo-France, 31100 Toulouse, France

Keywords: PolTomoSAR, Pol-InSAR, Foliage penetration, Ground Cancellation, Ground-notched InSAR

Abstract

Detecting objects hidden beneath a forest cover with Synthetic Aperture Radar (SAR) is challenging due to strong vegetation scattering, canopy attenuation, and ground returns. This work investigates two methods for detecting concealed targets using Polarimetric tomographic SAR (PolTomoSAR). The first approach exploits full-rank polarimetric tomographic focusing to achieve high-resolution separation of scattering sources and estimate their polarimetric responses. Target detection is then carried out using descriptors derived from decomposition techniques, such as the polarimetric entropy, and double-bounce scattering intensity, enabling the identification of man-made objects embedded within a dense vegetation layer. The second approach considers a compact configuration using only two interferometric SAR (InSAR) images. Coherent ground-notching suppresses the dominant ground scattering contribution, while preserving responses from above-ground scatterers. It is demonstrated that the baseline value plays a significant role in the detection process, and an optimum value is selected. Both methods are evaluated using L-band data set acquired by the DLR F-SAR over Dornstetten, Germany. Results demonstrate successful detection of concealed objects for varying baseline configurations.

1. Introduction

The detection of objects lying beneath a forest cover using Synthetic Aperture Radar (SAR) measurements represents a major challenge, due to complex scattering mechanisms from the overlying vegetation volume, wave attenuation caused by propagation through the forest canopy, and high-intensity scattering mechanisms occurring at the ground level (Ferro-Famil et al., 2015), (Davis, 2011). Traditional methods that rely solely on either tomography or polarimetry both face limitations when used independently. TomoSAR-based approaches provide 3D spatial information, which helps resolve cluttered environments, yet they often struggle with the complexities of polarimetric signatures that vary across different targets and conditions (Aguilera et al., 2013). In (Nannini et al., 2008), the forest profile and truck shape were both extracted using single polarization Capon’s method. However, due to the limited spectral resolution and sidelobe suppression of such an approach, fully polarimetric tomographic approaches are expected to show significantly improved features of under-foliage objects and forests (Huang et al., 2012). On the other hand, PolSAR-based methods can offer detailed insights into the scattering characteristics of objects but are limited by their inability to fully capture the vertical structure of the scene (Marino et al., 2012).
3D polarimetric SAR imaging, through Polarimetric tomographic SAR (PolTomoSAR), represents a promising solution to address these limitations, as it enables discriminating objects from their background by leveraging both polarimetric and spatial diversities (Tebaldini and Rocca, 2012). PolTomoSAR is based on the use of diversely polarized electromagnetic waves acquired from different trajectories. Its use permits to both improve the tomographic separation between different components of complex volumetric media and to characterize the EM behavior of the observed environments. In (Huang et al., 2013), isolated scatterer selection is applied to eliminate the volume effects of the canopy and detect underfoliage targets, and full-rank techniques, proposed in (Ferro-Famil et al., 2012), (Huang and Ferro-Famil, 2021), are used to extract more relevant physical features. These techniques have been used to extend the classical polarimetric processing from 2-D to 3-D.
While PolTomoSAR is effective in extracting detailed information, the polarimetric and radiometric features of strong ground-scattering contributions can often prevent the detection of above-ground objects when dealing with data that feature low vertical resolution. To address this problem, interferometric ground cancellation techniques, based on ground-notched InSAR processing, have been proposed to suppress the ground scattering and improve the sensitivity of SAR systems to above-ground biomass (Mariotti d’Alessandro et al., 2020). In the context of concealed object detection, the choice of the interferometric baseline separating the acquisition trajectories is crucial, as it balances the suppression of the forest canopy contribution and the preservation of responses from above-ground objects.
This work investigates two approaches based on PolTomoSAR processing, and adapted to different tomographic acquisition configurations, i.e. different vertical resolution and ambiguity compromises. The remainder of this paper is organized as follows. Section 2 introduces the principles of PolTomoSAR for forest characterization and under-foliage detection. In Section 3, concealed object detection is performed using various baseline configurations. First, a simple detector, combining a few source descriptors, such as the polarimetric entropy and indicators of double-bounce scattering, is proposed to effectively identify objects embedded in dense masking vegetation. This detector builds on full-rank PolTomoSAR focusing techniques, enabling high-resolution isolation of scattering sources located just a few meters above the ground, while also estimating their full-rank polarimetric responses. Next, an extreme but far less complex configuration is considered, consisting solely of a two-image PolInSAR acquisition. Ground-notched InSAR

This contribution has been peer-reviewed. The double-blind peer-review was conducted on the basis of the full paper.
https://doi.org/10.5194/isprs-annals-XI-3-2026-75-2026

processing is applied to suppress ground scattering contributions. Both methods are applied to a 21-image fully polarimetric L-band data set, acquired by the DLR F-SAR sensor over Dornstetten, Germany. Results are presented in Section 4. Finally, conclusions and perspectives are reported in Section 5.

2. Under-foliage Target PolTomoSAR Signal Model

SAR tomographic imaging (TomoSAR) is based on the acquisition of M SAR signals along slightly shifted trajectories, which together form an equivalent array. This spatial diversity is used to refine 2D resolution cells into 3D voxels, enabling the discrimination of echoes originating from scatterers located at different elevations. After focusing, compensating and co-registering the acquired signals, M 2D SAR images are obtained, $y(x_0, r_0)$, where x and r represent azimuth and slant range coordinates respectively. Following the formulation in (Bou et al., 2025), the content of the resolution cell of a 2D SAR image at the range-azimuth location (r_0, x_0) can be written as:

$$y(x_0, r_0) = \int_{C(x_0,r_0)} a(\mathbf{r}) e^{j\mathbf{k}_c \cdot \mathbf{r}} \, d\mathbf{r} + n(x_0, r_0), \quad (1)$$

where the 2D SAR impulse response is assumed to remain constant within the resolution cell, $\mathbf{r}$ is a 3D location, $a(\mathbf{r})$ is the complex reflectivity function and $\mathbf{k}_c$ is the two-way wave vector determined by the acquisition geometry. The integration takes place within the 3D resolution cell defined by $C(x_0, r_0)$, with $n(x_0, r_0)$ denoting the 2D focused acquisition noise. For natural environments, the coherent reflectivity density $a(\mathbf{r})$ is treated as a spatially white random field satisfying:

$$E(a(\mathbf{r})) = 0 \quad \text{and} \quad E(a(\mathbf{r})a^*(\mathbf{r} + d\mathbf{r})) = \sigma(\mathbf{r})\delta(d\mathbf{r}) \quad (2)$$

with $\delta()$ the Dirac function. Under the assumption of spatial stationarity in azimuth and range in high-resolution systems, $\sigma(\mathbf{r})$ in (2) becomes $f(z)$, a function of elevation only. Fig. 1 (a) illustrates the scattering mechanisms occuring in a forest with concealed objects. The SAR response in this case can be effectively modeled as the sum of three distinct components originating from the ground, the forest canopy, and the object beneath the vegetation, as illustrated in Fig. 1. These components being independent, the vertical density of reflectivity can be written as:

$$f(z) = f_g(z) + f_o(z) + f_v(z), \quad (3)$$

where $f_g(z)$, $f_o(z)$, and $f_v(z)$ denote the ground, object, and volume contributions, respectively. The cross-correlation between a pair of interferometric images can thus be expressed as:

$$I_{mn} = E(y_m y_n^*) = \int f(z) e^{j(k_{z_m} - k_{z_n})z} \, dz + \sigma_n^2 \delta_{m-n} \quad (4)$$

where k_{z_m} is the phase-to-relative height conversion coefficient of the m-th image, σ_n^2 is the noise variance, and δ_{m-n} is the discrete Dirac function. The covariance matrix can be defined as:

$$\mathbf{R} = E(\mathbf{y}\mathbf{y}^H) = \mathbf{A}\mathbf{P}\mathbf{A}^H + \sigma_n^2 \mathbf{I}_M \quad (5)$$

where $\mathbf{P} = \text{diag}(f(\mathbf{z}))$, with $\mathbf{z} = [z_1, \ldots, z_{n_s}]^T$ represents a sampled version of the reflectivity density. The steering matrix is given by

$$\mathbf{A}(\mathbf{z}) = [\mathbf{a}(z_1), \ldots, \mathbf{a}(z_{n_s})],$$

with $\mathbf{a}(z) = [1, \exp(jk_{z_2}z), \ldots, \exp(jk_{z_M}z)]^T$ the steering vector modeling multi-baseline interferometric phase information as a function of elevation z. In a PolTomoSAR configuration, each acquisition consists of a triplet containing the polarimetric response of the scene. The received signal may then be represented by rearranging the M acquired signals under the form of a $3M$ element vector, $\mathbf{y}_P$, containing 3 TomoSAR components, each related to a polarization channel:

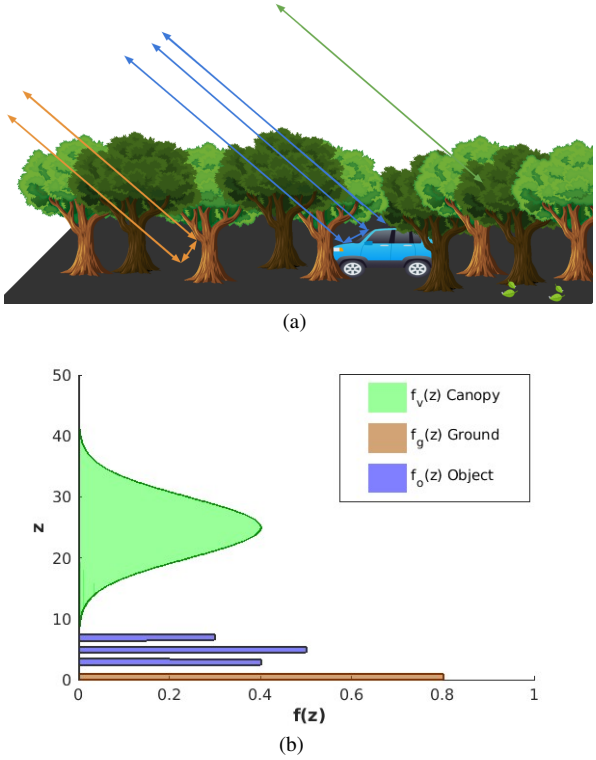

Figure 1. (a) Scattering mechanisms occurring in underfoliage target imaging. (b) Associated vertical reflectivity profiles

$$\mathbf{y} = \begin{bmatrix} \mathbf{y}_1^T & \mathbf{y}_2^T & \mathbf{y}_3^T \end{bmatrix}^T \in \mathbb{C}^{3M}$$

where $\mathbf{y}_p \in \mathbb{C}^M$, with $p = 1, 2, 3$, represents the TomoSAR response for the p-th polarimetric channel. The cross-correlation between two acquisitions for polarimetric channels p and q becomes:

$$E(y_{p_m} y_{q_n}^*) = \int f_{pq}(z) e^{j(k_{z_m} - k_{z_n})z} \, dz + \sigma_n^2 \delta_{m-n} \quad (6)$$

where $f_{pq}(z)$ is the polarimetric reflectivity density for these polarimetric channels. The full PolTomoSAR covariance matrix can be written, by generalizing (5), as:

$$\mathbf{R}_P = E\left(\mathbf{y}_P \mathbf{y}_P^H\right) = \sum_{k=1}^{n_s} \mathbf{T}(z) \otimes \mathbf{a}(z)\mathbf{a}^H(z) + \sigma_n^2 \mathbf{I}_{3M}$$

where $\mathbf{T}(z)$ is the polarimetric covariance matrix density along the elevation direction, with entries $\mathbf{T}_{mn}(z) = f_{mn}(z)$.

3. Concealed Object Detection with Various Baseline Configurations

This section presents two baseline configurations for concealed object detection: the first uses full-rank PolTomoSAR focusing for high-resolution separation of scattering sources, while the

second applies a compact InSAR configuration with ground-notching to suppress ground scattering and preserve above-ground responses.

3.1 Using Full-Rank PolTomoSAR focusing

3.1.1 Single-Polarization TomoSAR Spectral Estimators

The classical Beamformer and Capon spectral techniques provide an estimate of the reflectivity density as:

$$\hat{f}_B(z) = \frac{\mathbf{a}^H(z)\,\widehat{\mathbf{R}}\,\mathbf{a}(z)}{M^2}, \quad \hat{f}_C(z) = \left(\mathbf{a}^H(z)\,\widehat{\mathbf{R}}^{-1}\,\mathbf{a}(z)\right)^{-1} \tag{7}$$

where $\widehat{\mathbf{R}}$ denotes the L-look estimate of $\mathbf{R}$.

3.1.2 Full-Rank polarimetric Beamformer and Capon estimators

The Full-Rank Beamformer and Capon estimators are given in (Ferro-Famil et al., 2012):

$$P_{\text{B-FR}}(z) = \frac{\text{tr}(\mathbf{B}_\mathbf{a}^H(z)\widehat{\mathbf{R}}_P\mathbf{B}_\mathbf{a}(z))}{M^2} \tag{8}$$

$$P_{\text{C-FR}}(z) = \text{tr}\left(\left(\mathbf{B}_\mathbf{a}^H(z)\widehat{\mathbf{R}}_P\mathbf{B}_\mathbf{a}(z)\right)^{-1}\right) \tag{9}$$

with $\mathbf{B}_\mathbf{a} = I_{(3\times3)} \otimes \mathbf{a}(z_i)$. Once the 3D-coherency matrices are estimated from the full-rank PolTomoSAR processing, the concealed object detection is then conducted, based on polarimetric parameters provided by classical decomposition techniques: Polarimetric entropy (H) (Cloude and Pottier, 1996) and Double Bounce (DB) intensity from the Van Zyl decomposition.

3.1.3 Detection criterion based on polarimetric descriptors

A simple detector combining these source descriptors, proves effective in identifying artificial objects embedded in dense, masking vegetation. The detection rule can be formulated as follows:

$$D = \begin{cases} 1, & \text{if } \exists\ z_{min} < z < z_{max} \mid\ T(z) = 1 \\ 0, & \text{otherwise} \end{cases} \tag{10}$$

where $T(z_i)$ is defined as:

$$T(z) = \begin{cases} 1, & \text{if } H(z) < \tau_{\text{H}} \text{ and } DB(z) > \tau_{\text{DB}}, \\ 0, & \text{otherwise.} \end{cases} \tag{11}$$

Here, $H(z)$ denotes the polarimetric entropy and $DB(z)$ the double-bounce component estimated using the Van Zyl decomposition at height z, and τ_{H} and τ_{DB} are the empirically determined thresholds for entropy and double-bounce scattering, respectively. The detection operation corresponds to identifying all pixels where a target-like response is observed within a considered range of elevations. The rationale behind this detection rule is based on the complementary nature of the two features. Low entropy is indicative of more structured, coherent scattering, which is typically associated with targets such as vehicles, buildings, or other man-made structures, while high double-bounce scattering provides further confirmation of solid, structured objects, as double-bounce scattering is a common feature for such targets (Huang et al., 2013).

3.2 Using Interferometric Ground Notching

While TomoSAR imaging aims at spatially separate ground, object and canopy contributions after focusing in the vertical direction, coherent ground notching exploits the interferometric phase difference between the two SAR acquisitions to cancel signals coming from the ground while preserving those from scattering sources, including objects, located at other elevation coordinates. In practice ground-notching uses ground steering, which is achieved by adjusting the interferometric phase based on known or estimated ground height.

Let y_n and y_m denote two co-registered and ground-steered SAR images. The ground-notch image, y_{GN}, is defined as:

$$y_{\text{GN}} = \frac{1}{2}\left(y_n - y_m\, e^{-j\Delta k_{z_{nm}}(z-z_g)}\right). \tag{12}$$

Based on the signal model introduced in (4):

$$\begin{aligned} I_{\text{GN}} &= E\left(|y_{\text{GN}}|^2\right) \\ &= \int f(z)\sin^2\left(\frac{\Delta k_{z_{nm}}(z-z_g)}{2}\right)dz + \frac{\sigma_n^2}{2} \end{aligned} \tag{13}$$

The sinusoidal weighting in Equation (13) enforces suppression of echoes originating from $z = z_g + \frac{2n\pi}{\Delta k_z}$, $n \in N$, and emphasizes echoes originating from $z = z_g + \frac{2(n+1)\pi}{\Delta k_z}$, $n \in N$. Unlike applications centered around ground cancellation only, in the context of concealed object detection, the choice of the interferometric baseline separating the acquisition trajectories is crucial, as it balances the suppression of the forest canopy contribution and the preservation of responses from above-ground

4. Experimental results

4.1 Application dataset

The dataset used in this study was acquired near Dornstetten, Germany, at L-band in September 2006. Several reference targets (vehicles, containers, and corner reflectors) were deployed both inside and outside the forest to study the effect of canopy on target response. The test site is relatively flat, with about half of the area covered by heterogeneous forest stands of different species. Tree heights range from 10 to 30 m. The acquisition

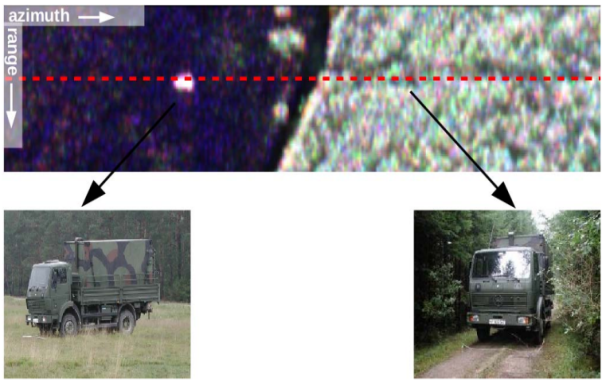

Figure 2. Dornstetten site. The test profile along which the processing is carried out is depicted in a red dashed line. It contains two trucks, one deployed in open ground (left) and one concealed beneath the canopy (right) - Courtesy Dr. Nannini, DLR.

followed a regular horizontal grid of 21 tracks with an average baseline of 20 m. The realized geometry closely matched the planned one, with deviations of up to 4 m (Nannini et al., 2008). Fig. 2 presents the relevant section of the fully polarimetric single-look complex (SLC) image in RGB coding (HH,

HV, VV). Tomographic processing was applied along the cut marked with dashed line in the image: It contains two trucks (one deployed in open ground and one concealed beneath the forest canopy).
The ground elevation map, used as a reference by both methods, was estimated using the method described in (Huang et al., 2013).

4.2 High vertical resolution acquisition

The Full-rank Beamforming (BF) and Capon estimators are applied to reconstruct the vertical scattering profiles and recover the polarimetric responses of the identified scatterers.
Fig. 3 shows the Full-rank SPAN tomograms, where SPAN = $I_{HH} + 2I_{HV} + I_{VV}$ (Cloude and Pottier, 1996), reconstructed using the Beamformer and Capon estimators.

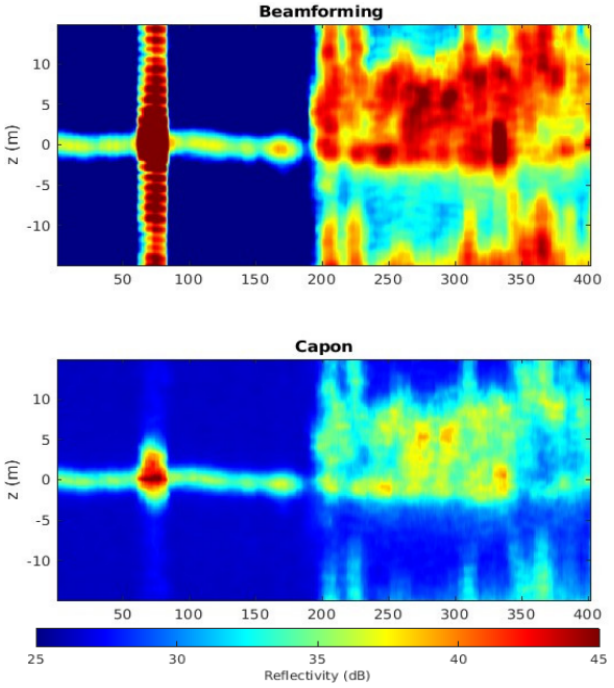

Figure 3. Full-rank SPAN Beamformer (top) and Capon (bottom) tomogram estimates for the selected profile (dB).

Both reconstructions clearly highlight the vehicle located on open terrain, appearing near the ground level. Importantly, the vehicle located beneath the forest canopy remains visible, confirming that the Full-rank PolTomoSAR processing retains scattering contributions associated with targets obscured by vegetation.

To characterize the scattering behavior along elevation, the polarimetric entropy H was evaluated for several reconstructed height slices. Fig. 4 shows the entropy maps for elevations $z = 0$, 1, 2, and 3 m. The vehicle on open ground maintains consistently low entropy across all elevations, indicating stable dominant scattering. The concealed vehicle remains detectable with low entropy up to approximately $z \approx 2$ m, but becomes indistinguishable at $z = 3$ m due to the stronger volume scattering introduced by the forest canopy. Fig. 5 shows the double-bounce intensity estimated from the Van Zyl decomposition (Van Zyl et al., 2011). The open-ground vehicle exhibits a strong double-bounce component, as expected for dihedral-type

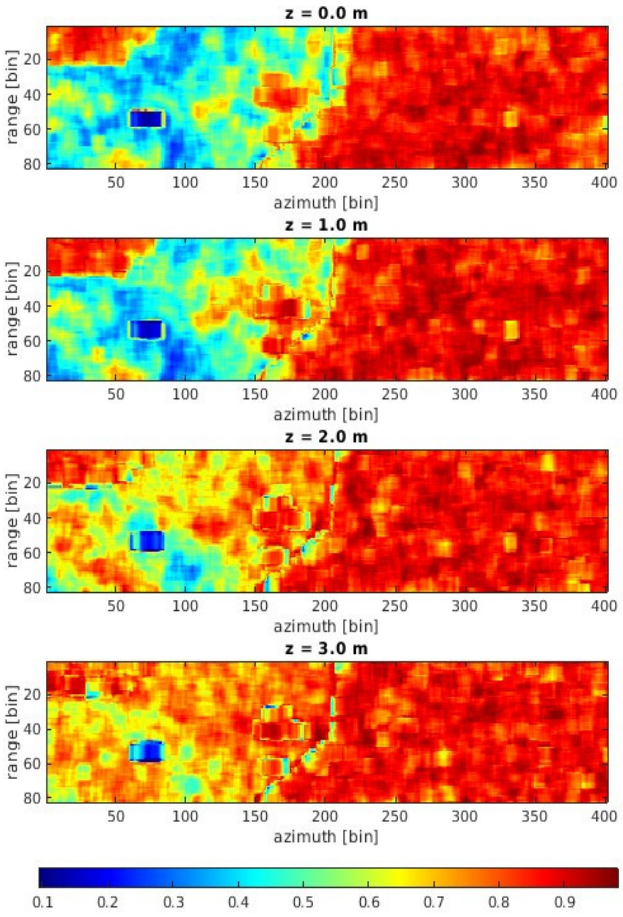

Figure 4. Full-rank BF polarimetric entropy maps at several elevations above the ground.

metallic targets. The concealed vehicle also exhibits a detectable double-bounce peak up to $z \approx 2$ m, confirming its structural nature despite canopy interference. Finally, the detector combining low entropy and high double-bounce scattering was applied to produce the detection map shown in Fig. 6. Both objects remain clearly identifiable from 0 m to 2 m. The detector correctly identifies both vehicles, including the one concealed under forest canopy, demonstrating the effectiveness of the full-rank PolTomoSAR processing in target detection.
The peformance of the detection method is illustrated in Fig. 7 which shows the overlap ratio as a function of the false detection rate across 170 combinations of entropy and double bounce intensity threshold values, $\tau_H \in [0.1,\ 0.9]$ and $\tau_{DB} \in [40,\ 50]$. For each combination, the overlap ratio is calculated as the fraction of the target area that is detected, while the false detection rate is defined as the empirical probability of detecting pixels that do not belong to target areas. Optimal threshold values were selected to balance a high overlap ratio, larger than 60%, with a low level of false detection rate, smaller than $4e-3$.
The previous results were obtained using a Full-rank PolTomoSAR configuration, involving a large number of baselines and providing both high vertical resolution and a wide unambiguous elevation range. While this configuration yields highly informative 3D reconstructions, it is also complex and data-demanding.

4.3 Low vertical resolution acquisition

In this section, a compact configuration consisting of only two polarimetric interferometric SAR images (PolInSAR) is con-

This contribution has been peer-reviewed. The double-blind peer-review was conducted on the basis of the full paper.
https://doi.org/10.5194/isprs-annals-XI-3-2026-75-2026 | © Author(s) 2026. CC BY 4.0 License.

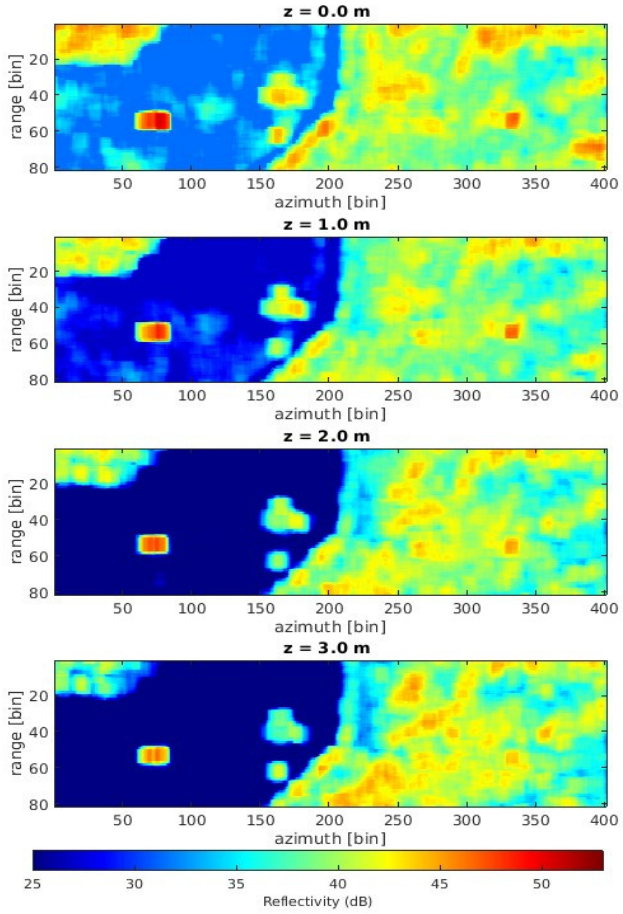

Figure 5. Double-bounce scattering intensity esimated by the VanZyl decomposition for the selected area (dB).

sidered. No full tomographic inversion is possible, and elevation discrimination relies entirely on the interferometric phase diversity between the two acquisitions. To enhance target visibility and suppress the dominant ground contribution, ground-notching is performed. Fig. 8 (b) shows the resulting ground-notched intensity image for the test profile.

Despite the severely reduced elevation information compared to the full tomographic configuration, the ground-notched image effectively suppresses the dominant ground layer, allowing the signature of concealed targets to emerge more distinctly.

The parameter Δk_z directly controls the vertical frequency of the sinusoidal weighting applied by the ground notch. As a result, it determines which elevation layers are suppressed and which are emphasized. When Δk_z is small (Fig. 8 (a)), the notching function varies slowly with height, resulting in a broad attenuation pattern that suppresses most of the vertical components of the scene. In this case, both the canopy and the weak target responses are strongly attenuated, leading to an overall loss of information. Conversely, a large Δk_z produces a rapidly oscillating notching function, which enhances the separation between scatterers at different heights (Fig. 8 (b)). This configuration allows a clearer restitution of above-ground targets, but also preserves contributions from the understorey and canopy, which may partially mask the objects of interest. Hence, selecting an appropriate Δk_z value is essential to balance the suppression of dominant ground scattering while maintaining sufficient sensitivity to the desired targets.

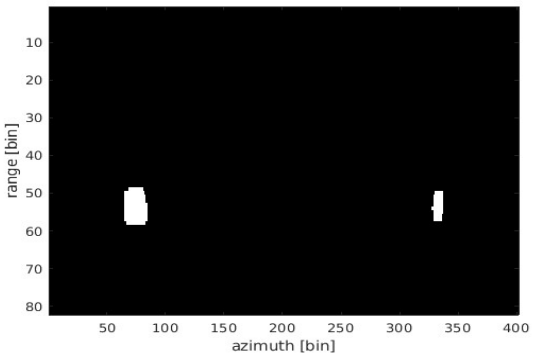

Figure 6. PoltomoSAR object detection results, with $\tau_H = 0.7$ and $\tau_{DB} = 46$.

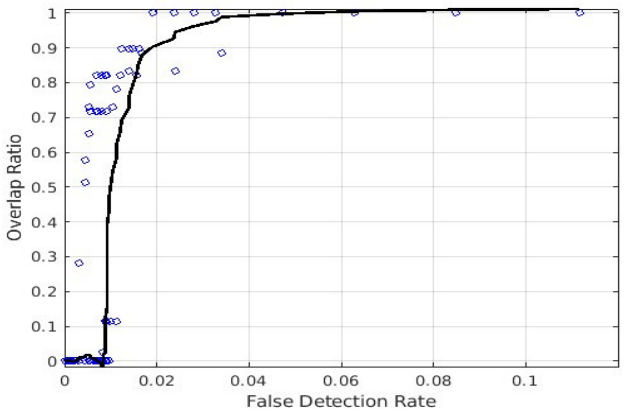

Figure 7. Overlap ratio vs false detection rate.

Finally, the detection map for the case of a large Δk_z variation is shown in Fig. 9.

4.4 Computational Complexity

From a computational perspective, both Ground notching and conventional Beamforming exhibit comparable behavior, as they rely on simple linear operations followed by spatial smoothing. Ground notching primarily involves subtraction between images to suppress ground clutter, while Beamforming consists of a weighted combination of multiple images with subsequent smoothing. In contrast, the Capon method is more computationally demanding, since it requires adaptive weight estimation based on the inversion of the data covariance matrix having $N_{im} * N_{pol} = 63$ rows.

5. Conclusion

This study presented two complementary approaches for the detection of concealed targets under forest cover using Polarimetric SAR Tomography (PolTomoSAR) at L-band. The first method, based on full-rank tomographic focusing, demonstrated the ability to isolate scattering mechanisms and identify objects characterized by low entropy and strong double-bounce responses. The second method, relying on a compact two-image configuration and ground-notched InSAR processing, effectively suppressed ground scattering while preserving the polarimetric signatures of above-ground objects. Experiments on the Dornstetten data set confirmed that both methods can reveal vehicles and containers hidden beneath dense vegetation. The

This contribution has been peer-reviewed. The double-blind peer-review was conducted on the basis of the full paper.
https://doi.org/10.5194/isprs-annals-XI-3-2026-75-2026 | © Author(s) 2026. CC BY 4.0 License.

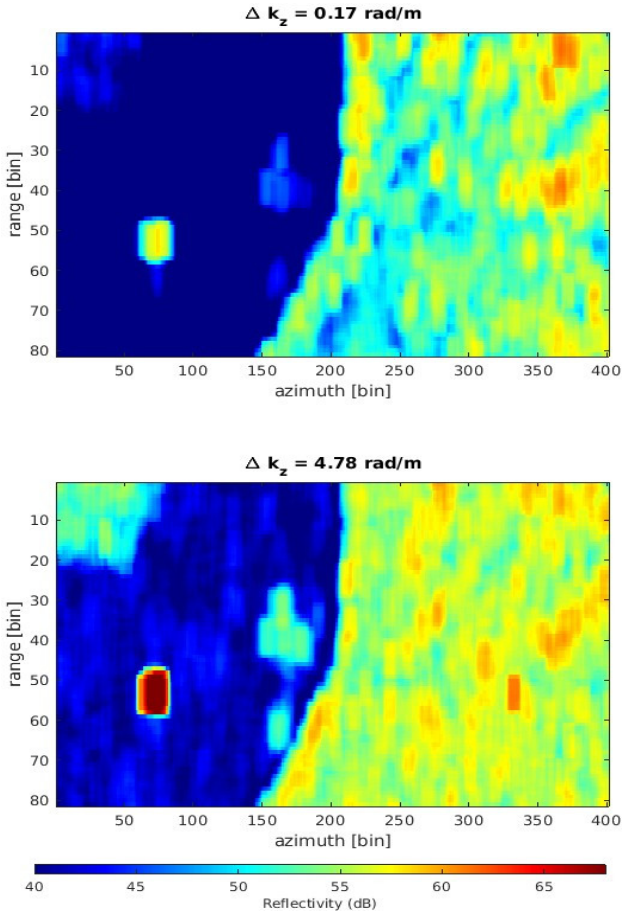

Figure 8. Ground notched intensity maps for different Δk_z (a) - $\Delta k_z = 0.17$. (b) - $\Delta k_z = 4.78$

results highlight the trade-off between vertical resolution and acquisition complexity, showing that reliable detection can be achieved even with a minimal number of passes. Future work will focus on extending the ground-notched processing to adaptive Beamforming and Capon-based approaches for operational applications requiring reduced data volumes and faster processing.

6. Acknowledgment

The work reported in this paper was supported by DGA-AID under Project DOCTOSAR-3DFOR 2022-65-0082.

References

Aguilera, E., Nannini, M., Reigber, A., 2013. Wavelet-Based Compressed Sensing for SAR Tomography of Forested Areas. *IEEE Transactions on Geoscience and Remote Sensing*, 51(12), 5283-5295.

Bou, P.-A., Ferro-Famil, L., Brigui, F., Huang, Y., 2025. Tropical Forest Characterization Using Parametric SAR Tomography at P Band and Low-Dimensional Models. *IEEE Geoscience and Remote Sensing Letters*, 22, 1-5.

Cloude, S., Pottier, E., 1996. A review of target decomposition theorems in radar polarimetry. *IEEE Transactions on Geoscience and Remote Sensing*, 34(2), 498-518.

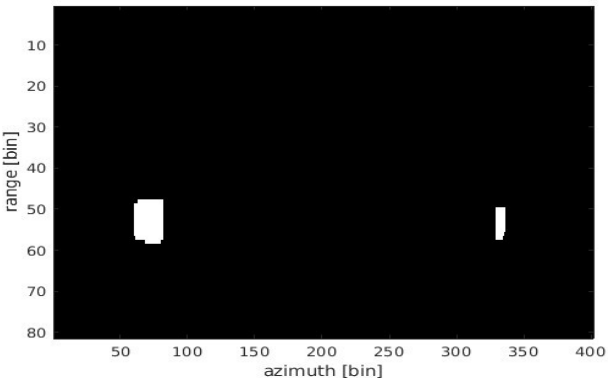

Figure 9. Concealed object detection map obtained by ground-notching and $\Delta k_z = 4.78 rad/m$.

Davis, M., 2011. *Foliage Penetration Radar: Detection and characterisation of objects under trees*.

Ferro-Famil, L., Huang, Y., Pottier, E., 2015. Principles and applications of polarimetric SAR tomography for the characterization of complex environments. *VIII Hotine-Marussi Symposium on Mathematical Geodesy: Proceedings of the Symposium in Rome, 17-21 June, 2013*, Springer, 243–255.

Ferro-Famil, L., Huang, Y., Reigber, A., 2012. High-resolution SAR tomography using full rank polarimetric spectral estimators. *2012 IEEE International Geoscience and Remote Sensing Symposium*, 5194–5197.

Huang, Y., Ferro-Famil, L., 2021. 3-D Characterization of Urban Areas Using High-Resolution Polarimetric SAR Tomographic Techniques and a Minimal Number of Acquisitions. *IEEE Transactions on Geoscience and Remote Sensing*, 59(11), 9086-9103.

Huang, Y., Ferro-Famil, L., Reigber, A., 2012. Under-Foliage Object Imaging Using SAR Tomography and Polarimetric Spectral Estimators. *IEEE Transactions on Geoscience and Remote Sensing*, 50(6), 2213-2225.

Huang, Y., Ferro-Famil, L., Reigber, A., 2013. Under-foliage target detection using multi-baseline L-band PolInSAR data. *2013 14th International Radar Symposium (IRS)*, 1, 449–454.

Marino, A., Cloude, S. R., Woodhouse, I. H., 2012. Detecting Depolarized Targets Using a New Geometrical Perturbation Filter. *IEEE Transactions on Geoscience and Remote Sensing*, 50(10), 3787-3799.

Mariotti d’Alessandro, M., Tebaldini, S., Quegan, S., Soja, M. J., Ulander, L. M. H., Scipal, K., 2020. Interferometric Ground Cancellation for Above Ground Biomass Estimation. *IEEE Transactions on Geoscience and Remote Sensing*, 58(9), 6410-6419.

Nannini, M., Scheiber, R., Horn, R., 2008. Imaging of targets beneath foliage with SAR tomography. *7th European Conference on Synthetic Aperture Radar*, 1–4.

Tebaldini, S., Rocca, F., 2012. Multibaseline Polarimetric SAR Tomography of a Boreal Forest at P- and L-Bands. *IEEE Transactions on Geoscience and Remote Sensing*, 50(1), 232-246.

Van Zyl, J. J., Arii, M., Kim, Y., 2011. Model-based decomposition of polarimetric SAR covariance matrices constrained for nonnegative eigenvalues. *IEEE Transactions on Geoscience and Remote Sensing*, 49(9), 3452–3459.